REVIEW OF SCIENTIFIC INSTRUMENTS VOLUME 75, NUMBER 9 SEPTEMBER 2004

A three-dimensional electron spin resonance microscope

Aharon Blank, Curt R. Dunnam, Peter P. Borbat, and Jack H. Freed[a)]
National Biomedical Center for Advanced ESR Technology, Department of Chemistry and Chemical Biology, Cornell University, Ithaca, New York 14853

(Received 26 January 2004; accepted 3 June 2004; published 15 September 2004)

An electron spin resonance (ESR) imaging system, capable of acquiring three-dimensional (3D) images with a resolution of $\sim 10\times 10\times 30\ \mu$m in a few minutes of acquisition, is presented. This ESR microscope employs a commercial continuous wave ESR spectrometer, working at 9.1 GHz, in conjunction with a miniature imaging probe (resonator+gradient coils), gradient current drivers, and control software. The system can acquire the image of a small ($\sim 1.5\times 1.5\times 0.25$ mm) sample either by the modulated field gradient method, the projection reconstruction method, or by a combination of the two. A short discussion regarding the resolution of the modulated field gradient method in two-dimensional (2D) and 3D imaging is given. Detailed descriptions of the various system components are provided, along with several examples of 2D and 3D images that demonstrate the capabilities of the system.
[DOI: 10.1063/1.1786353]

I. INTRODUCTION

Magnetic resonance is one of the most useful imaging methodologies in materials science, biology, and medicine.[1–3] While "traditionally" most of the applications of this technique have been associated with nuclear magnetic resonance (NMR) imaging, some of the more recent investigations have been carried out by electron spin resonance (ESR) imaging. The main ESR imaging (ESRI) efforts have been directed towards the observation of large biological objects and the determination of their radical and oxygen concentrations (by their effect on the radical linewidth).[4–7] Such experiments, conducted *in vivo*, employ low fields of $\sim$10 mT at low rf frequencies (which results in relatively low spin sensitivity), in order that the rf energy will penetrate deeply into the biological object. Consequently, a typical voxel resolution in low frequency ESR experiments is $\sim[2\ \text{mm}]^3$. A different approach attempts to examine much smaller objects, with better spatial resolution. This type of ESRI, directed towards microscopy (analogous to a NMR microscope[8]), can be employed at higher frequencies with improved sensitivity. Previous efforts in ESR microscopy (ESRM) are scarce, and have resulted in an achievable resolution of $\sim 25-100\ \mu$m for two-dimensional (2D) and three-dimensional (3D) imaging.[9–12] We recently achieved 2D images with a resolution of $\sim[10\ \mu\text{m}]^2$ by employing continuous wave (cw) ESR imaging utilizing a unique probe design.[13]

At present, ESRM is still far less developed (mainly due to technological issues) than NMR microscopy, for which commercial instruments can provide 3D resolution of $\sim 10-20\ \mu$m in small biological samples.[8] Nevertheless, ESR has many virtues compared to NMR, which should make it the technique of choice with respect to magnetic resonance imaging in many microscopic applications. For example, the signal per spin in ESR is much greater than in NMR,[14] diffusion does not limit the resolution in the short time scales (T_1, T_2's $\leqslant 10\ \mu$s) of the ESR measurements, unlike NMR,[15–18] ESR microresonators have a quality factor (Q) of $\sim$1000 compared to a $Q\sim 10$ of the NMR microcoils,[8,19] and the ESR line shape is more sensitive to dynamic effects—leading to richer information.[20,21] An additional factor is the lower cost of electromagnets used in ESR as compared to the expensive superconducting magnets of NMR. These fundamental advantages, along with recent advances in ESR resonators, ESR spectrometer hardware, and paramagnetic contrast solutions, warrant the development of a micron resolution ESR-based microscope to overcome the resolution limitations of NMR microscopy and to provide complementary information to optical imaging modalities.

Our recent publication[13] described several potential applications for ESRM. It discussed in detail the theory and the limiting factors of current ESRM technology, and it presented some initial cw 2D imaging results performed with a high-permittivity miniature X-band (9.1 GHz) imaging probe. In the present work we discuss in detail the 3D cw microscope, which we have now developed. It is based on an improved microstrip-fed high permittivity resonator, a more efficient 3D imaging gradient coils set, and improved control software. The sophisticated hardware and software design of the microscope enables one to acquire the image either by the modulated field gradient (MFG) method[22,23] or through the projection reconstruction (PR) imaging method.[4,24] The microimaging system, suitable for use as an accessory with many pre-existing X-band cw ESR spectrometers, provides magnetic resonance imaging capability with a voxel resolution down to $\sim 10\times 10\times 30\ \mu$m in a few minutes of acquisition. To demonstrate the capability of the system, we show some imaging results for a solid sample of LiPc (Lithium Phthalocyanine radical) and for a solid form and a liquid

---

[a)] Author to whom correspondence should be addressed; electronic mail: jhf3@cornell.edu

suspension of the synthesized LiNc–BuO (lithium octa-*n*-butoxy-substituted naphthalocyanine radical) microparticulates.[25]

II. IMAGING METHOD

As noted above, the system can employ two different imaging methods to obtain the ESR image, within the framework of cw acquisition. Some of the results presented in this article were obtained with the PR method, which is probably the most common method used to acquire *in vivo* cw ESR images. This tomographic imaging technique has been described in detail in many previous publications,[26] and we shall not elaborate on it in this article. Other results presented here were collected employing the MFG method. This method is less commonly employed since it is mainly advantageous for microscopic applications. The MFG method has been described previously,[13,22,27] with discussions of the image acquisition technique, image signal-to-noise-ratio (SNR), and gradient coil requirements. Nevertheless, we include here, for clarity, a short outline of this method, and also present a discussion of image resolution in 2D and 3D imaging, as a function of the modulated field gradient amplitude, since this subject was not treated in previous publications.

The idea behind the MFG method is to over-modulate the entire imaged sample, apart from a single voxel, from which the ESR signal is obtained.[22] The over-modulation of the sample is achieved by a set of gradient coils excited by a low frequency periodic current. These coils have a null field point that can be swept in space by changing the relative current amplitude in each coil pair that produces the gradient field. Let us analyze more quantitatively the imaging scenario and obtain the image resolution for various cases. The time domain cw ESR signal in the case of conventional field modulation is given by[14]

$$S(t,B_\delta) = S_0 \frac{1}{\left(\frac{\Delta B_{1/2}}{2}\right)^2 + (B_\delta + B_m \sin \omega_m t)^2}, \tag{1}$$

where $\Delta B_{1/2}$ is the full width half maximum (FWHM) of the ESR line; $B_\delta = (B - B_0)$, where B_0 is the center of the line; B_m is the modulation field amplitude (at a frequency of, e.g., 100 kHz). The addition of sinusoidal modulation fields, whose amplitudes depend both on time and the spatial location, results in the following spatial/time domain signal

$$S(x,y,z,t,B_\delta) = S_0 \frac{1}{\left(\frac{\Delta B_{1/2}}{2}\right)^2 + [B_\delta + B_m \sin\ \omega_m t + B_z^x(x) \sin \omega_x t + B_z^y(y) \sin(\omega_y t + \varphi_y) + B_z^z(z) \sin(\omega_z t + \varphi_z)]^2}. \tag{2}$$

The modulated field gradients for the X, Y, and Z axes $-B_z^x$, B_z^y, B_z^z, and of course the main modulation field, B_m, are all in the direction of the laboratory Z axis (determined by B_0). The field B_m is assumed to be homogeneous over the entire sample volume (i.e., without any spatial dependence). The modulated field gradients are employed at much lower frequency (e.g., 10–1000 Hz), and have the following spatial dependence:

$$B_z^x(x) = xG_x, \tag{3}$$

$$B_z^y(y) = yG_y,$$

$$B_z^z(z) = zG_z.$$

It is thus clear that at the origin, where $(x,y,z) = (0,0,0)$, Eq. (2) simplifies to Eq. (1). At other locations however, the ESR signal is greatly attenuated, due to the over-modulation induced by the modulated gradients, and this attenuation increases as the voxel is more distant from the origin. As mentioned above, the origin (null field point) can be moved by changing the ratio of the currents in the pairs of coils, which generate the modulated field gradients. The entire image is obtained by electronically scanning the imaged voxels within the sample volume.

We shall now address the issue of image resolution. Qualitatively speaking, it is clear that the image resolution should be finer as G_x, G_y, and G_z increase. In addition, the gradient modulation frequencies ω_x, ω_y, ω_z, the relative phases between the gradient modulation (φ_y, φ_z), and also the time constant of the cw ESR signal acquisition affect the image resolution. In order to provide quantitative analysis of these factors, we examine the ESR signal harmonics (with respect to the main modulation frequency). These harmonics are detected by the cw ESR spectrometer and are given (for the pth harmonic) by[14]

$$a_p = \int_{t=0}^{T} S(x,y,z,t,B_\delta) \sin(p\omega_m t)\, dt. \tag{4}$$

If $B_z^x = B_z^y = B_z^z = 0$, then each harmonic signal has a specific field, $B_\delta = B_\delta^m$, for which it is maximal (for example, for the second harmonic signal, $B_\delta^m = 0$). As one increases B_z^x, B_z^y, and/or B_z^z, the amplitude of a_p at B_δ^m will decrease and quickly reach zero.[22] To calculate the image resolution, for a specific signal harmonic p, we first find the field B_δ^m and then increase B_z^x, B_z^y, and/or B_z^z (depending on the dimensionality), in our numerical calculations of a_p, until a_p at B_δ^m becomes zero. The values of B_z^x, B_z^y, and/or B_z^z for which $a_p = 0$, divided by the applied gradient [Eq. (3)], provide us with the image resolution. This resolution criterion is analogous to the Rayleigh criterion for resolution in optics.[28]

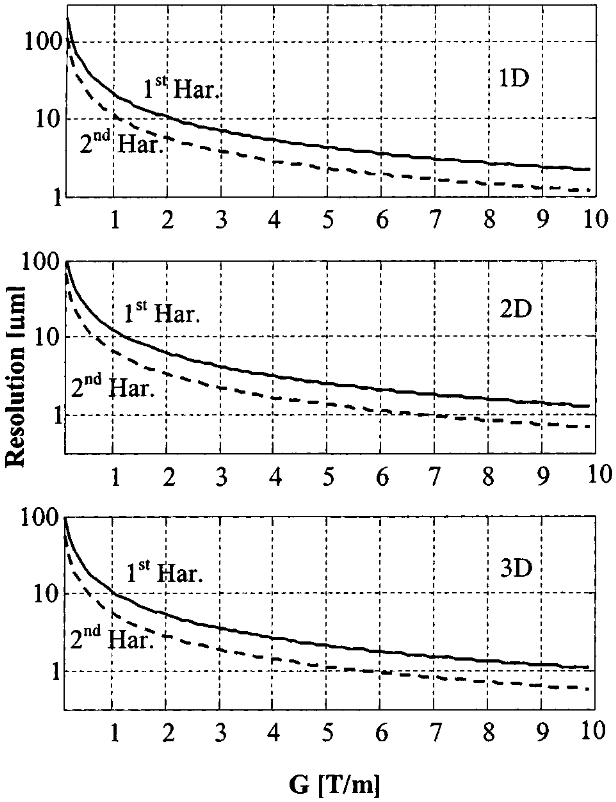

FIG. 1. Calculated image resolution for one, two, and three dimensions, employing the MFG method for the first (solid line) and second harmonics (dashed line) of the cw ESR signal. The FWHM radical linewidth and B_m are assumed to be 0.01 mT for all cases. The calculation assumes the same applied gradient in all imaged dimensions.

The calculations of the resolution were performed numerically for several representative cases, and the results are shown in Fig. 1. We assumed for purposes of this analysis that $\omega_x = \omega_y = \omega_z$, (although the system can support different frequencies for the X, Y, and Z gradient coils, see below). Also $G_x = G_y = G_z = G$, and the integration time, T, in Eq. (4) was taken as the period time of ω_x. The relative phases, φ_y, and φ_z, are determined according to the dimensionality of the problem: When increasing the dimensionality of the image (e.g., from 1D to 2D), every point in space experiences the added fields of more than one coil pair. This can lead to "interference effects" as shown for the 2D example in Figs. 2(a) and 2(b), which show how strong image artifacts are created if $\varphi_y = 0$, since the resolution depends on the direction taken from the null point. To avoid such artifacts, one should apply a phase difference between the modulated fields of the different axes. In the 2D calculation of Fig. 1, we employed an optimal $\varphi_y = 90°$, and in the 3D example we applied $\varphi_y = 120°$, $\varphi_z = 240°$. This approach tends to minimize the spatial dependence of the resolution (i.e., image artifacts) by averaging out the positive and negative interference effects [cf. Figs. 2(c) and 2(d)]. Similar artifact cancellation can be achieved by employing different modulated gradient frequencies for each axis. Both methods (i.e., phase and/or frequency variation among the imaging axes) can be employed in our imaging system (see below).

III. CONTINUOUS WAVE ESR MICROSCOPE

The cw ESR microscope has the following components (Fig. 3): (a) Conventional cw ESR spectrometer; (b) dedicated computer which controls the imaging process and acquires the ESR signal; (c) current drivers for the gradient coils; (d) base band (up to ~250 kHz) amplifier and filter unit (signal conditioner); (e) control unit; (f) imaging probe that includes the microwave resonator, mechanical fixture for holding the sample, and gradient coils. We shall first describe an overview of the imaging procedure and the manner by which the microscope is operated. This provides the overall perspective before describing, in detail, the functionality and characteristics of each of the main components of the microscope system.

To image a sample, one must first attach the imaging probe (Fig. 4) to the cw ESR spectrometer (by replacing the conventional resonator). The imaging probe is connected to the spectrometer through the microwave (MW) input/output of the spectrometer and the modulation coils line (similar to any cw-ESR resonator). In addition, the probe is connected to the gradient current drivers and to air and water cooling lines. The water and air cooling lines are essential to maintain a stable resonance frequency of the high permittivity resonator [Fig. 4(b)]. The investigated sample should be sealed (under normal or deoxygenated atmosphere) between two flat glass cover slips and inserted, with the help of the sample holder, to an exact position in the center of the resonator. Following this, the ESR spectrometer is set to acquire the signal of the sample at the required conditions of MW power, dc magnetic field, and main modulation. After fixing the spectrometer on the maximum of the ESR signal, the computer controlled imaging procedure is initiated, and the gradient coils are activated to obtain the image (see below). The ESR microscope incorporates a field frequency lock (FFL) system that adjusts the dc magnetic field by biasing the modulation coils of the imaging probe, and maintains the on-resonance condition throughout the period of the imaging experiment. Thus, the basic commercial cw ESR spectrometer is completely "unaware" of the imaging procedure, with the interfaces between the spectrometer and the imaging probe/system being kept to a minimum. The image is displayed on the computer in real time during the acquisition process and then can be saved and/or manipulated as necessary.

Following this introductory description, we now relate more details of the individual components of the 3D cw ESR imaging system:

(a) Continuous wave ESR spectrometer. As mentioned above, most commercial cw ESR spectrometers (e.g., from Bruker, Varian, or JEOL) can be used as a basis for the imaging module. The spectrometer serves as a good stable, amplitude controlled, MW source that is independently frequency locked on the resonance frequency of the imaging probe, by means of the spectrometer automatic frequency control (AFC). The spectrometer also provides a current drive for the regular modulation coils of the imaging probe and should allow for the operator to fix the external dc magnetic field close to the resonance field of the imaged sample.

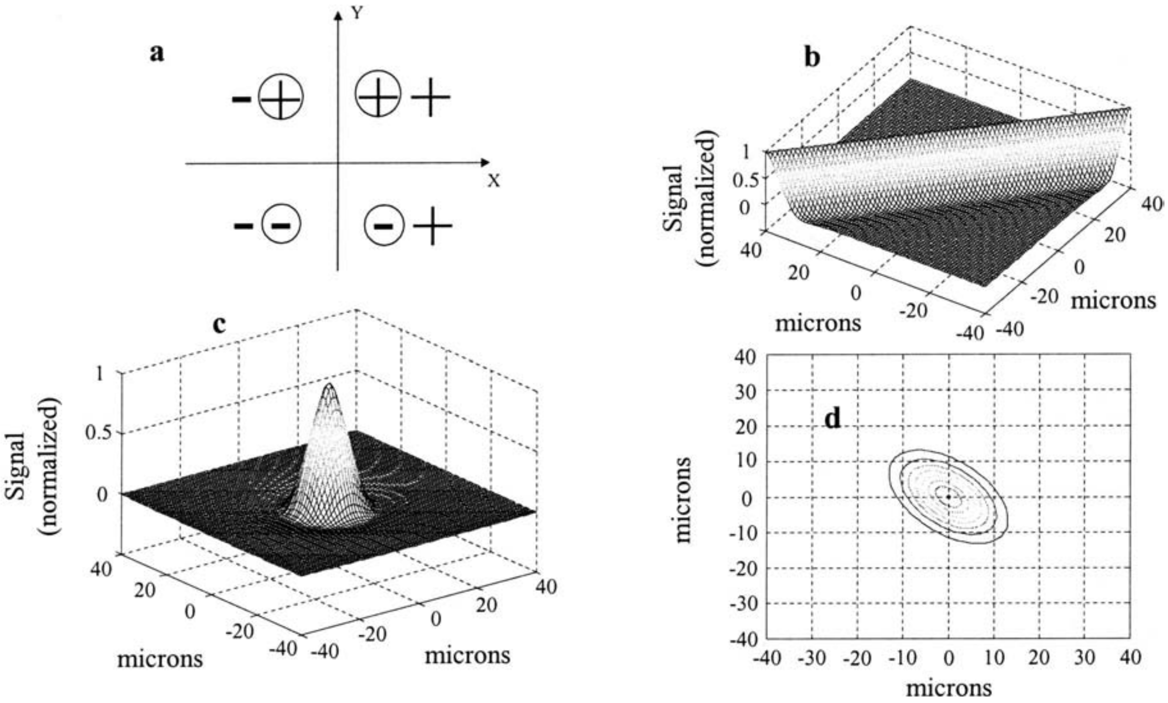

FIG. 2. (a) The effect of two modulated field gradients applied for the *x* and *y* axes simultaneously. The fields due to the *x* coil pair are marked with ± without circles and the fields due to the *y* coil pair are marked with ± with surrounding circles. It can be seen from the figure that if $\varphi_y=0$, then the modulated fields will be stronger in the first and third quadrants, while tending to cancel each other in the second and fourth quadrants. (b) Image of a point target with infinitely small size situated at the origin of axes (point spread function) for 2D MFG, assuming $\varphi_y=0$. Parameters used in this calculation are: linewidth of 0.01 mT, $B_m=0.01$ mT, $G_x=G_y=1$ T/m. It is obvious that such a point spread function will result in bad artifacts in the image. (c) The same as (b), but with $\varphi_y=90°$. This phase difference between the *x* and *y* gradients leads to the minimization of the artifacts in the point spread function. (d). A 2D cut through the 3D point spread function, which involved the simultaneous application of *x*, *y*, and *z* gradients. The phase difference of 120° between each axis minimizes the image artifacts but still causes an appreciable anisotropy in the point spread function, which corresponds to some unavoidable anisotropic artifacts in the 3D MFG method.

The MW ESR signal returning from the imaging probe is detected and preamplified at the spectrometer MW bridge. In our spectrometer (Varian E-12), we inserted prior to the diode detection of the ESR signal from the resonator a low noise *X*-band preamplifier (Miteq AFS3-08001200-14-ULN). This amplifier improves the SNR of the spectrometer by a factor of ~5 and its amplification gain (~25 dB) enables the AFC of the Varian bridge to lock on the returning signal even for low MW power (~1 μW), that is common in our imaging experiments (see below). The diode detected base band signal is directly fed from the bridge preamplifier (similar to the case of time resolved ESR measurements[29]) to a signal conditioning unit and then goes to the PC for sampling and further analysis (see below).

(b) Control computer and imaging software: The entire imaging process is controlled by a standard PC equipped with two analog input+digital input/output (I/O) (National Instruments 6023E) and analog output (National Instruments 6713) cards. These cards enable arbitrary wave form generation and fast sampling of signals up to several hundred kHz. The digital analysis of the sampled diode detected ESR signal supersedes the need to employ a conventional lock-in amplifier while simultaneously obtaining all the ESR signal harmonics, in the correct phase, with respect to the main modulation current.[13,30] The current software version of the system is capable of acquiring 2D images at any given *z* location (3D slice selection). The 2D imaging methods that can be employed are either the PR or the MFG method. Both methods can in principle employ the MFG method for the *Z* slice selection (see below). It should be noted that the hardware (probe+current drivers) also supports 3D imaging with projection reconstruction and 4D spectral-spatial projection reconstruction that can be pursued in the future by updating the imaging control software. The control software (based on LABVIEW) obtains the imaging parameters from the user. These parameters include, for example, the number of pixels in the image (*x* and *y*), the current amplitude in the gradient coils, the wave form and frequency used in the modulated gradient coils (e.g., sine, serrasoid, etc.), the image extent in mm, and parameters related to the functionality of the FFL system. The software can also acquire the normal ESR signal (first and second harmonics), by sweeping the magnetic dc

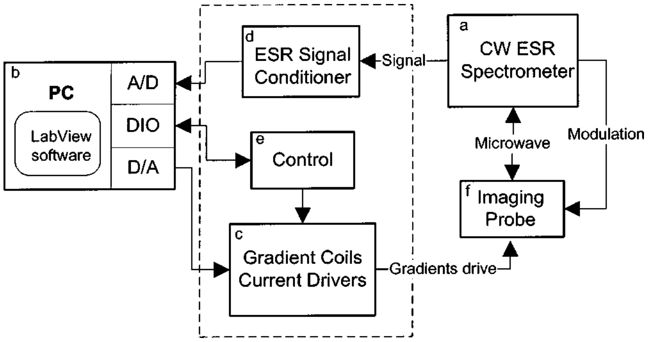

FIG. 3. Block diagram of the 3D cw ESR microscope.

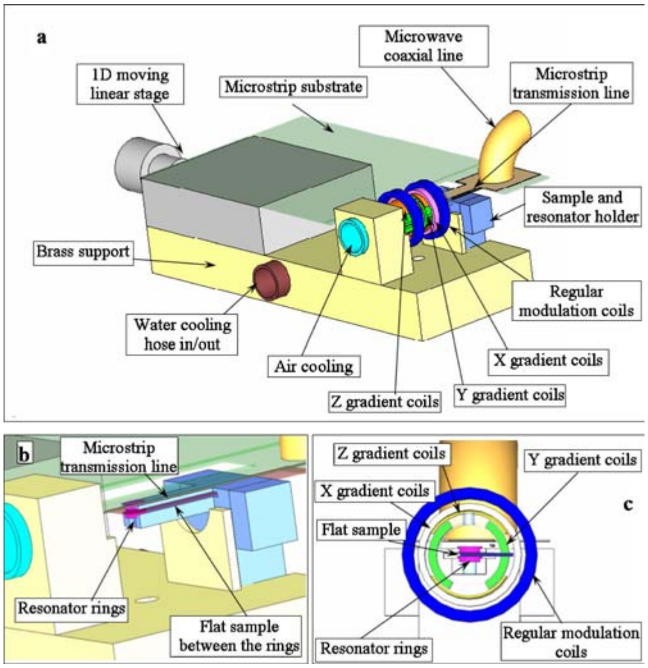

FIG. 4. (Color online) The cw imaging probe. (a) General layout of the probe. (b) A closer look at the resonator (purple) and Delrin sample and resonator holder (light blue) when the various modulation coils are removed. (c) The probe structure examined from the direction of the air cooling hose, showing the layout of the modulation coils with respect to the resonator rings.

field with the probe's gradient coils. At the end of the imaging process the data can be saved and/or further processed with the aid of MATLAB software. Such postprocessing includes, for example, in the case of image acquisition through the PR method, de-convolution of the projections, and inverse Radon transformation[31] to obtain the image.

(c) Current drivers for the gradient coils: The gradient coils are driven by six programmable current sources (one for each coil) each capable of supplying up to 3 A of arbitrary wave form current, in the dc-10 kHz range. Each current driver is based on a simple feedback loop, and its electronic schematic is shown in Fig. 5. In practice, the coils in the present system do not require more than 1 A to generate high enough gradient fields. The low current consumption of the system greatly simplifies the design and space requirements for the driver unit.

(d) Base band amplifier and filter unit (signal conditioner): In most ESR spectrometers, the ESR signal, detected by the MW diode, goes through a base band preamplifier that is part of the commercial bridge. The signal level after this preamp is not large enough to be sampled directly by the analog/digital (A/D) card in the computer. To facilitate proper A/D sampling we employ a signal conditioning unit comprised of bandpass filters and a high gain amplifier. The dual bandpass filter transfers only signal at the regular modulation frequency generated by the cw spectrometer, and its second harmonic. For example, in our present system we have a filter that transfers 25 and 50 kHz and the spectrometer is operated at 25 kHz modulation frequency. The high gain amplifier (Tektronix AM502) that follows the dual bandpass filter produces variable gain (manually controlled) in the range of 40–100 dB.

(e) Control unit: The current wave form in the gradient coils can be generated either directly at the computer analog output card or in the control unit. This unit receives commands from the computer via the 8 bit digital I/O bus of the 6023E card and consequently synthesizes the required wave forms. The control unit is limited in the complexity of the wave form it can generate (as compared to the arbitrary wave form generator of the analog output card), but for most imaging tasks it has sufficient capabilities. Its important virtue

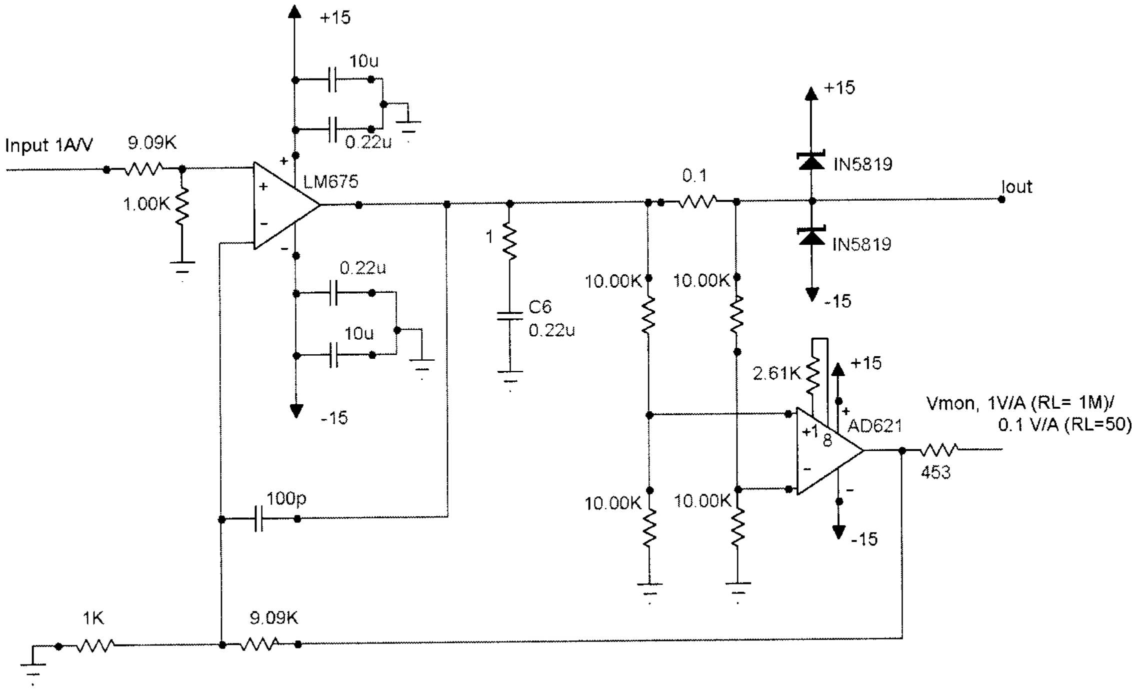

FIG. 5. Circuit diagram of the wave form current driver of the gradient coil.

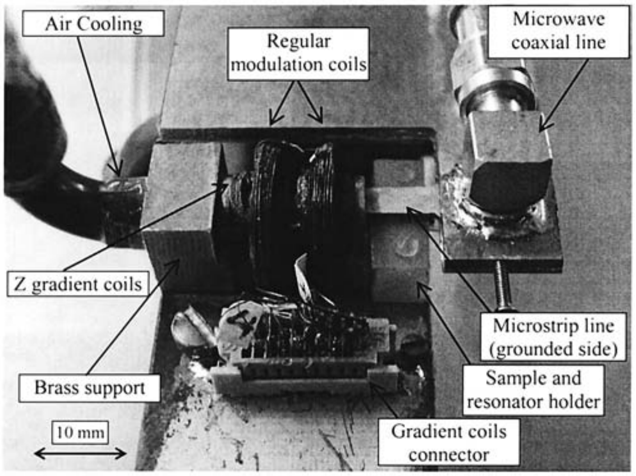

FIG. 6. Photo of the cw imaging probe. The resonator rings and the microstrip excitation line are not visible, since the rings are inside the gradient coils shield and the excitation line is facing down. The *X* gradient coils are right below the regular modulations coils and the *Y* gradient coils are below the *Z* gradient coils.

is that it reduces the overhead time in the imaging procedure related to the calculation and generation of the different wave forms in the computer and thus shortens the actual acquisition time by a factor of ~2.

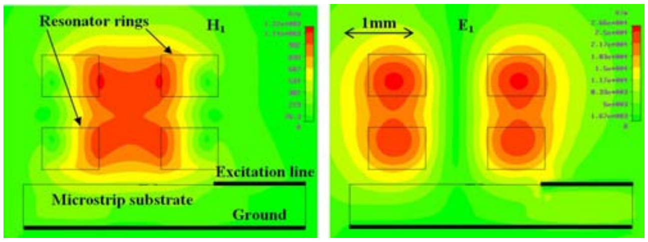

FIG. 7. (Color online) The calculated microwave magnetic (H_1) and electric (E_1) fields of the resonating mode of the high-permittivity resonator, for the case of microstrip excitation.

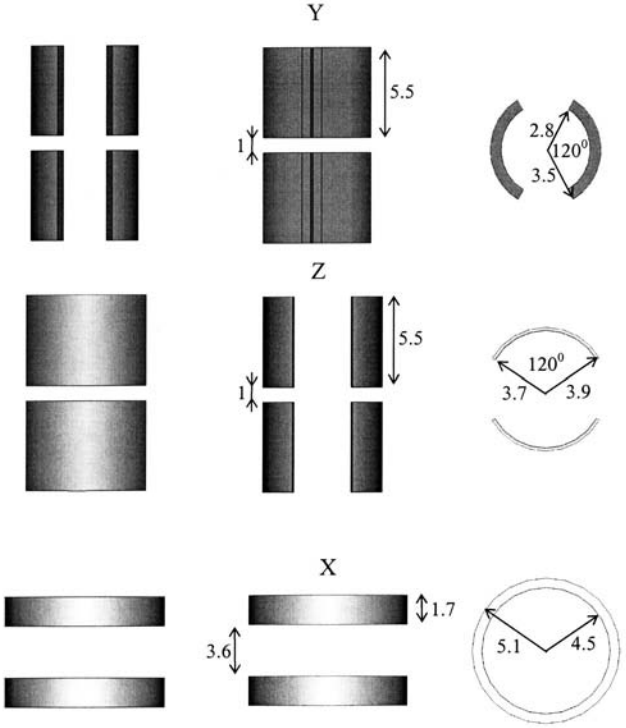

FIG. 8. The geometry of the gradient coils in the three axes. Dimensions are in mm. Main modulation coils (not shown) are a Helmholtz pair separated by 5 mm with a radius of 6 mm.

(f) Imaging probe: The imaging probe is the heart of the cw imaging system. A schematic drawing of the imaging probe is given in Fig. 4, and a photo of the actual probe is in Fig. 6. The probe is based on a double stacked ring resonator,[13,19,32] machined from $SrTiO_3$ single crystal (Commercial Crystals, FL). This crystal has permittivity of ~300 at room temperature and $\tan\delta \sim 5\times10^{-4}$. Each one of the resonator rings is 0.55 mm in height with outer diameter of 2.31 mm and inner diameter of 0.81 mm. When the two rings were placed at a separation of ~0.4 mm, the fundamental resonance frequency of this structure was found to be ~9.15 GHz (in the center of the working frequency of the Varian E-12 ESR spectrometer). The resonator is excited by a microstrip transmission line on a low-loss substrate (GE electromaterials GTEK ML200D Epoxy/Polyphenylene Oxide resin). The excitation geometry and the calculated fields of this resonator at the resonance frequency (CST Microwave Studio) are shown in Fig. 7. The "effective volume" of the resonator,[13] as derived from the calculated magnetic fields is ~3 mm^3 for ring separation of 0.4 mm. The two high permittivity rings are held by a Delrin part at a fixed distance [Fig. 4(b)]. This Delrin spacer also holds the flat sample and enables exact positioning of the imaged object in the center of the resonator. Variable coupling is achieved by changing the distance between the resonator rings and the microstrip line using a linear 1D stage (nonmagnetic model MDE 255 from Elliot Scientific, GB). In addition, the vertical position of the rings with respect to the microstrip line can be varied slightly by moving the Delrin part up and down and/or adjusting the vertical microstrip line position. This variability enables optimal control of the rings' coupling for a wide variety of samples.

The resonator rings are surrounded by a thin (0.12 mm thick) hollowed brass cylinder that shields the resonator at the microwave frequencies, but is transparent to the low frequency magnetic field gradients (Fig. 8). The regular modulation of the cw spectrometers (commonly at 25–100 kHz) penetrates through the shield opening along the cylinder axis. The loaded *Q* of the resonator was found to degrade slightly, from ~1200 to ~900, when inserting it into the brass shield. The gradient *X*, *Y*, and *Z* coils are arranged around the cylindrical shield, along with the regular modulation coils (Fig. 8). The gradient coils are made from bondable 38 AWG copper magnet wire, and the modulation coils are made from bondable 32 AWG wire. The innermost coils are the *Y* and *Z* gradient coils, respectively, which are based on a "Golay" design.[33] The *X* gradient coils (standard Maxwell pair[33]), are positioned in the outermost layer of the gradient coils, followed by the main modulation Helmholtz pair (not shown in Fig. 8). Gradient efficiency is 4, 5, and 1.2 $\mathrm{T}/(m\times A)$, and coil resistance is 9, 8.5, and 4.4 Ω for the *X*, *Y*, and *Z*, coils, respectively. These figures significantly improve upon our

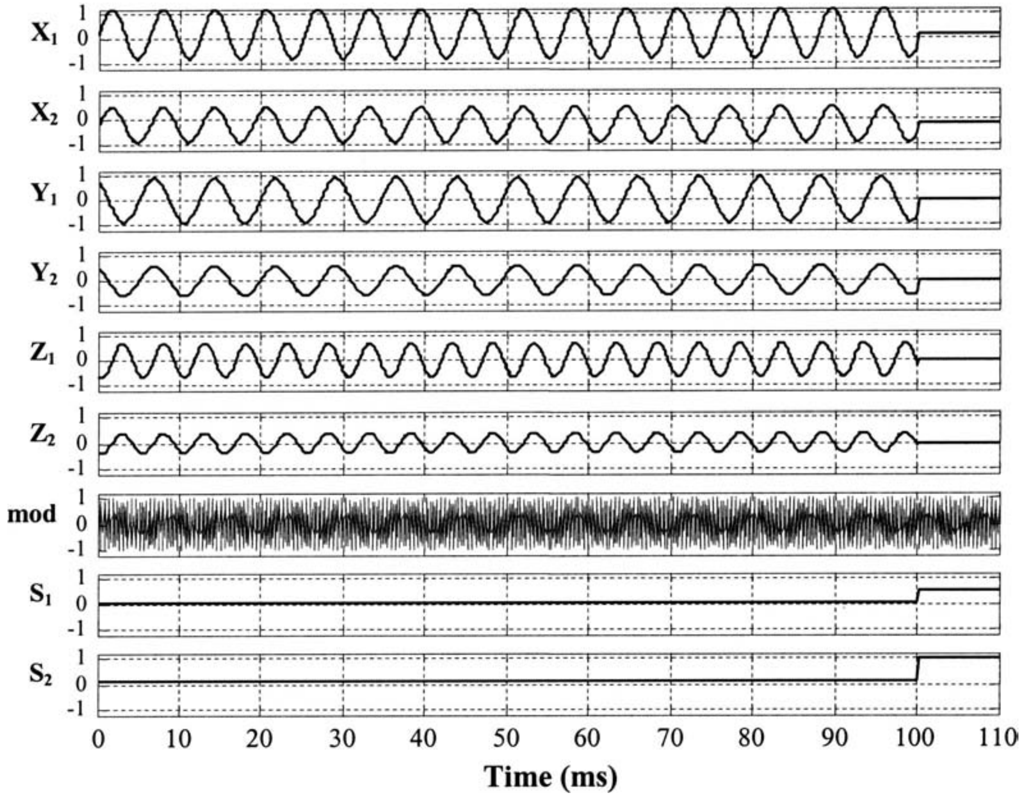

FIG. 9. Typical representative input and output signals for 3D modulated field gradient (MFG) imaging experiment with FFL control. The graphs show the current in the gradient coils (channels $X_1, X_2, Y_1, Y_2, Z_1, Z_2$), the regular modulation coils (mod) and the resulting first and second harmonics ESR signals (S_1 and S_2 respectively). The modulated gradient coils operate at a typical frequency of ~10–200 Hz. Each axis may have its own distinct frequency or relative phase (to control and avoid image artifacts, as referred to in the text of Sec. II). The current ratio between the amplitudes of the coil pairs (for example, X_1/X_2) determines the position of the null field for that specific pair while the current amplitude of both coils determines the resolution of that axis. At the end of the acquisition period of a single voxel (100 ms in this example), the system must pause for a while to process the data, update the output buffer of the computer/controller, and observe the signal without any modulation to correct for any frequency/field variation (the FFL mechanism). Notice that the current in the gradient coils is set to zero at the "rest" period to observe the bulk sample signal. The current in the X_1 coils is not zero since it includes a common-mode dc bias employed for the FFL field corrections (that is also why the sine modulation of this coil pair is offset from zero). The FFL correction mechanism relies on the first harmonic signal, S_1 (which should be zero at resonance), while the image signal is obtained from the second harmonic signal S_2, during the modulation period.

previous 2D probe design, which achieved gradient efficiency of ~1.5 and 2.5 $\mathrm{T}/(m\times A)$, for the Y and X coils respectively, with coil resistance of 8 Ω.[13]

The probe structure is cooled by water flow, which maintains the entire brass structure at constant temperature. In addition, the rings themselves are cooled by air or He flow to maintain a stable resonance frequency, since the $SrTiO_3$ is highly sensitive to temperature changes (at X band the drift is ~20 MHz per °K[34]). In principle, the water/air flow system can be temperature controlled to regulate the temperature in the range (~0–50 °C), but this is yet to be implemented within the current system. The imaging probe can accommodate flat samples with dimensions of ~1.5×1.5 mm (corresponding to the active area/volume of the probe, cf. Fig. 7) and a height of up to ~0.5 mm (depending on the separation of the resonator rings). In practice, for liquid samples, one should contain the sample in a glass structure. We found it useful to employ thin cover slips with a small acid etched "well," as a convenient container for the liquid samples. Such a design enables one to measure a net sample size of ~1.5×1.5 mm and a height of ~0.25 mm. These samples can be sealed, if necessary, under argon atmosphere, by the use of UV curable glue.

The spin sensitivity of the imaging probe was measured with a 1 mM deoxygenated water solution of protonated trityl radical.[35] A SNR of 1.6×10^4 was obtained for a 0.06 μL sample, with 1 s time constant and ~0.2 G field modulation. This SNR is in good agreement with the results of our recent publication (cf. Fig. 1 therein),[13] which predict a SNR of 1.8×10^4 for such a trityl sample. The measured SNR corresponds to a spin sensitivity of $\sim2.2\times10^9$ spins/$\sqrt{\mathrm{Hz}}$, and a concentration sensitivity of $\sim6.2\times10^{-8}$ M/$\sqrt{\mathrm{Hz}}$, for the flat sample considered here. The combination of high spin and concentration sensitivities, for samples of small volume, is essential to facilitate high resolution imaging capability.

Imaging procedure: At the beginning of this section we outlined the imaging process from the perspective of the operator of the system. The actual processes that occur "behind the scenes" are more involved and warrant some discussion. Two representative examples are described schematically for the MFG and the PR imaging methods in the form of time lines (Figs. 9 and 10). These examples, which are detailed in the figure captions, represent the flexibility and capability of the present system. As noted above, the hardware and soft-

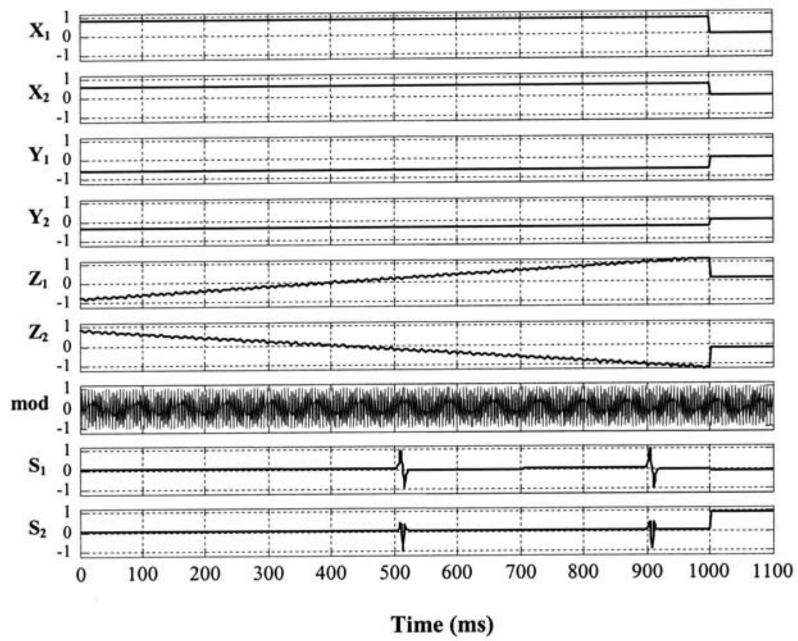

FIG. 10. Typical representative input and output signals for 2D/3D projection reconstruction (PR) imaging experiment with FFL control. The signal notation is as in Fig. 9. The X and Y coil pairs provide a gradient along a specific angle $(\tan\phi = Y_1/X_1)$. The current within a certain coil pair (for example X_1 and X_2) is not necessarily equal. This enables one to shift the origin in the XY plane. The scan of the dc magnetic field (to obtain the projection) is performed with the Z coils. For optional Z-slice selection by the modulated field gradient method, one can superimpose a sinusoidal wave form on top of the scan Z field, (as seen schematically in this figure, the superimposed modulated field is at a typical frequency of $\sim 10-200$ Hz). In addition, in this case the Z coil pair also compensates for field drifts (FFL) so the wave form of these coils also has some dc bias superimposed. As in the previous case, at the end of the scan (or possibly several times within the scan, if the scan is long) the acquisition process pauses for a while to obtain the un-modulated/zero gradient signal from the sample and to correct the FFL accordingly. The signals S_1 and S_2 show a typical projection for a sample made of two small point-like radical grains.

ware support any arbitrary excitation of the gradient coils (within the bandwidth of up to ~ 10 kHz). Thus, further progress in the direction of, for example, spectral-spatial imaging or 3D projection reconstruction may be pursued in the future with just software updates.

IV. EXPERIMENTAL RESULTS AND DISCUSSION

We now describe and discuss some representative experimental results of images acquired with the microscope system. These experiments, performed with solid and liquid samples, enable us to quantify the resolution, SNR, and image quality obtained in 2D and 3D measurements with the MFG and the PR methods. Imaging of the same samples with the two methods provides a good basis for comparison and discussion about their different advantages and disadvantages. Whenever applicable, the experimental results are compared to prior estimations of image SNR and resolution obtained by cw ESR imaging.[13,26]

(a) LiPc phantom: As a first example we measured a high spin concentration sample of solid LiPc crystal (the same crystal that was measured in our recent publication[13]). Figure 11 provides the measured 2D and 3D images of this crystal. The 2D images (Figs. 11(a) and 11(b)), were acquired with both the PR and the MFG methods. The image SNR (max signal from a voxel divided by the rms of the noise in areas of the image where no radicals are present) was found to be ~ 110 and ~ 240 for the MFG and PR methods, respectively. These figures can be compared with our theoretical estimates of image SNR,[13] and the spin sensitivity of the probe described above. The radical concentration is $\sim 10^{20}$ spins in 1 cm^3[36] (provided that the material density is ~ 1), which implies that there are $\sim 8\times 10^{11}$ spins in an image voxel of $10\times 10\times 80$ μm (see below). We know that $Q\sim 1000$, and the resonator active volume is ~ 3 mm^2 (see above) and we also assume T_1 and T_2 values similar to that of 1 mM trityl radical in water solution.[13] All these parameters result in an estimated SNR of ~ 150 for the MFG method [employing Eq. (5) in our recent publication,[13] and considering the second harmonic signal]. The PR method devotes longer acquisition time to each pixel (128 projections with sampling time of 20 ms as compared to 0.5 s per pixel in the MFG).[26] It also uses the stronger first harmonic signal ($\sim$two times larger than the second harmonic signal[14]), to simplify the de-convolution process.[26] These two factors should provide a SNR of the PR method, which is $\sim 4.4[=2\times(128\times 0.02/0.5)^{1/2}]$ times larger than that of the MFG method. In practice we obtained a PR SNR that is 2.2 times larger, probably due to image artifacts (see below) that contribute to the PR image apparent noise. Accurate absolute predictions of the image SNR (and the ESR signal in general) are somewhat problematic and the present results provide relatively good agreement with the theoretical predictions, both for the absolute SNR values, and the relative SNR between MFG and PR methods. These SNR results are also compatible with the measured probe spin sensitivity described in the previous section.

In terms of image resolution, analyzing the ESR images by taking a 1D cut at certain locations[13,37] [Fig. 11(a)] reveals that the resolution is $\sim 10\times 10$ μm for the 2D images acquired with both methods, and ~ 30 μm for the z slice separation in the 3D images (the latter number is less reliable due to the difficulty of accurately measuring the crystal Z dimension, which is estimated to be ~ 80 μm).[38] The theoretical resolution of the MFG method for 2D imaging was discussed above (cf. Fig. 1). The image in Fig. 11(a) involves gradients of 1 T/m, radical linewidth of 0.01 mT, and main modulation field of 0.015 mT, which results in the calculated 2D resolution of 9.5 μm (for the second harmonic signal). The PR method, which observes the first derivative signal, requires gradients that are about two times stronger to obtain a similar resolution.[26,39] In the present case, we obtained for the PR image a similar resolution (10 μm) to that of the MFG method with gradients of just 1.5 T/m, thanks to the use of de-convolution methods[26] to further sharpen the im-

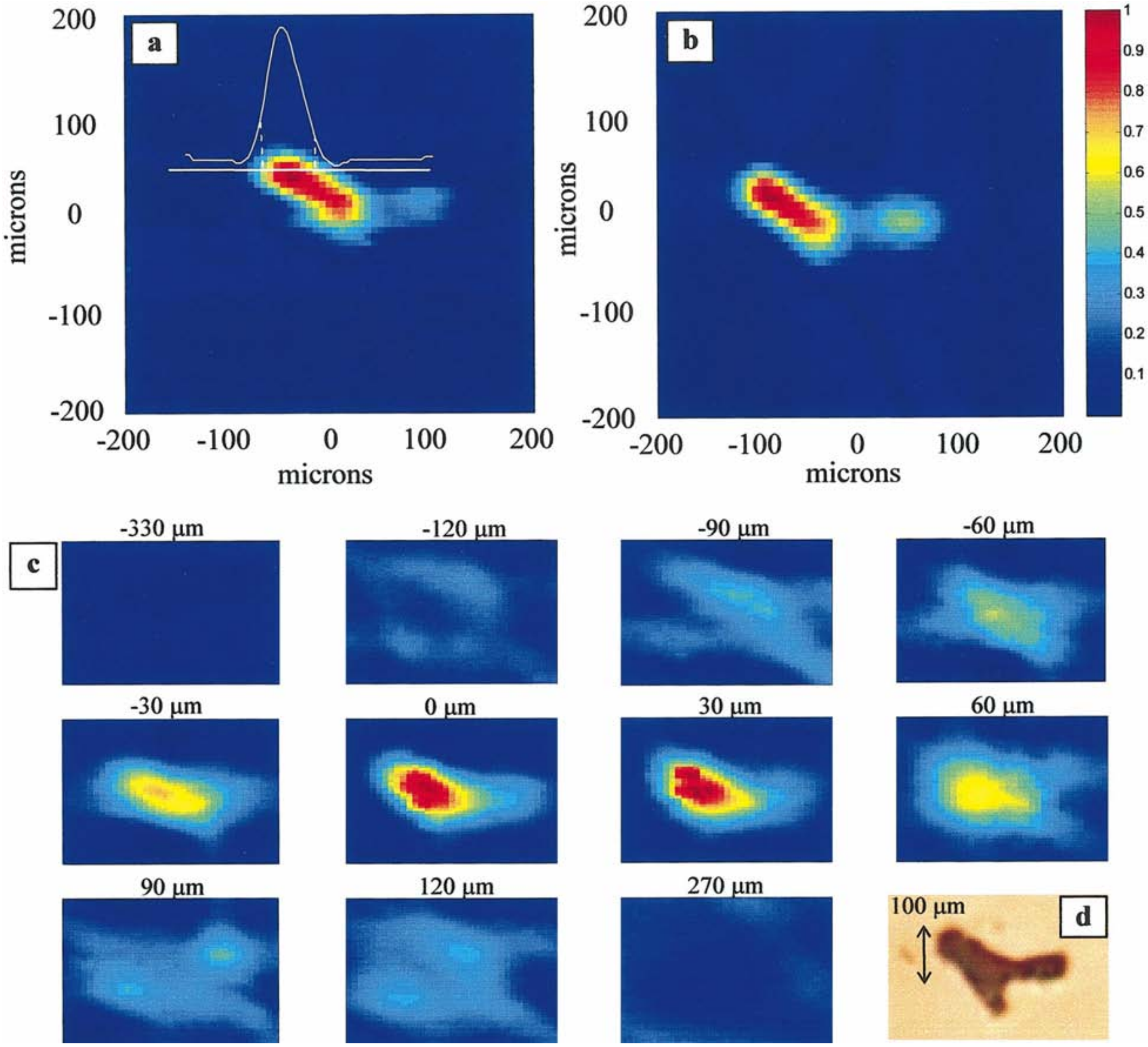

FIG. 11. (Color) ESR images of LiPc crystal. (a) A 2D ESR image employing the modulated field gradient method. The *XY* gradient magnitudes were 1 T/m. Image acquisition $(64 \times 64$ pixels$)$ of the second harmonic ESR signal took 34 min (time constant of 0.5 s). The superimposed white curve shows a 1D cut through the 2D image (obtained along the straight white line), which can be used to estimate the image resolution, by examining how far the signal extends beyond the optical image of the object (marked by the dashed lines, see Ref. 38). (b) A 2D ESR image employing projection reconstruction method. The *XY* gradient magnitudes were 1.5 T/m. Image acquisition (128 samples in projection and 128 projections at 0–360°) of the first harmonic signal took 6 min (20 ms for each sample). The vertical color bar represents the relative pixel ESR signal in arbitrary scale (different scale for the PR and MFG images). (c) A series of 2D images for different *Z*-slice selections acquired by the MFG method (similar acquisition parameters as in the 2D image). The coordinate of the selected *Z* slice is shown for every image. *Z* gradient was ~0.4 T/m. This series of images clearly demonstrate the ability to achieve good *Z*-slice separation at a resolution of ~30 μm. The images obtained correspond well to the estimated crystal *Z* dimension of ~80 μm. (d) Optical microscopy image of the examined LiPc crystal. All ESR images were acquired with a microwave power of 4 μW (larger power causes saturation of this sample in our resonator, see Ref. 13.), and field modulation of ~0.015 mT.

age. One additional important issue that should be discussed is related to image artifacts. In the MFG method image artifacts are mainly due to the negative wings of the point spread function [Figs. 2(c) and 2(d)] associated with this method and result in a negative signal surrounding the edges of the object. For the PR method, image artifacts tend to create “lobes” coming out of the object,[26] which contribute more significantly to the overall effective noise of the image.

Notice that the 2D ESR images do not correspond exactly to the optical image. This may be caused by (1) an inhomogeneous distribution of spins within the phantom (corresponding to the weak signal on the right side). In addition, (2) application of cyanoacrylate glue, during sample preparation, destroyed some of the radicals in the lower part of the phantom. The very similar results using both ESR imaging methods reinforces our belief that the ESR images are correct, and it shows that the optical image and ESR image do not have to be the same (as one would expect), since they measure different properties.

(b) LiNc–BuO radical:[25] This material, termed lithium octa-*n*-butoxy-substituted naphthalocyanine radical (LiNc–BuO), can be applied to biological samples *in vivo/in vitro* as a high concentration microparticulate liquid suspension.[25] The linewidth of this radical increases significantly with in-

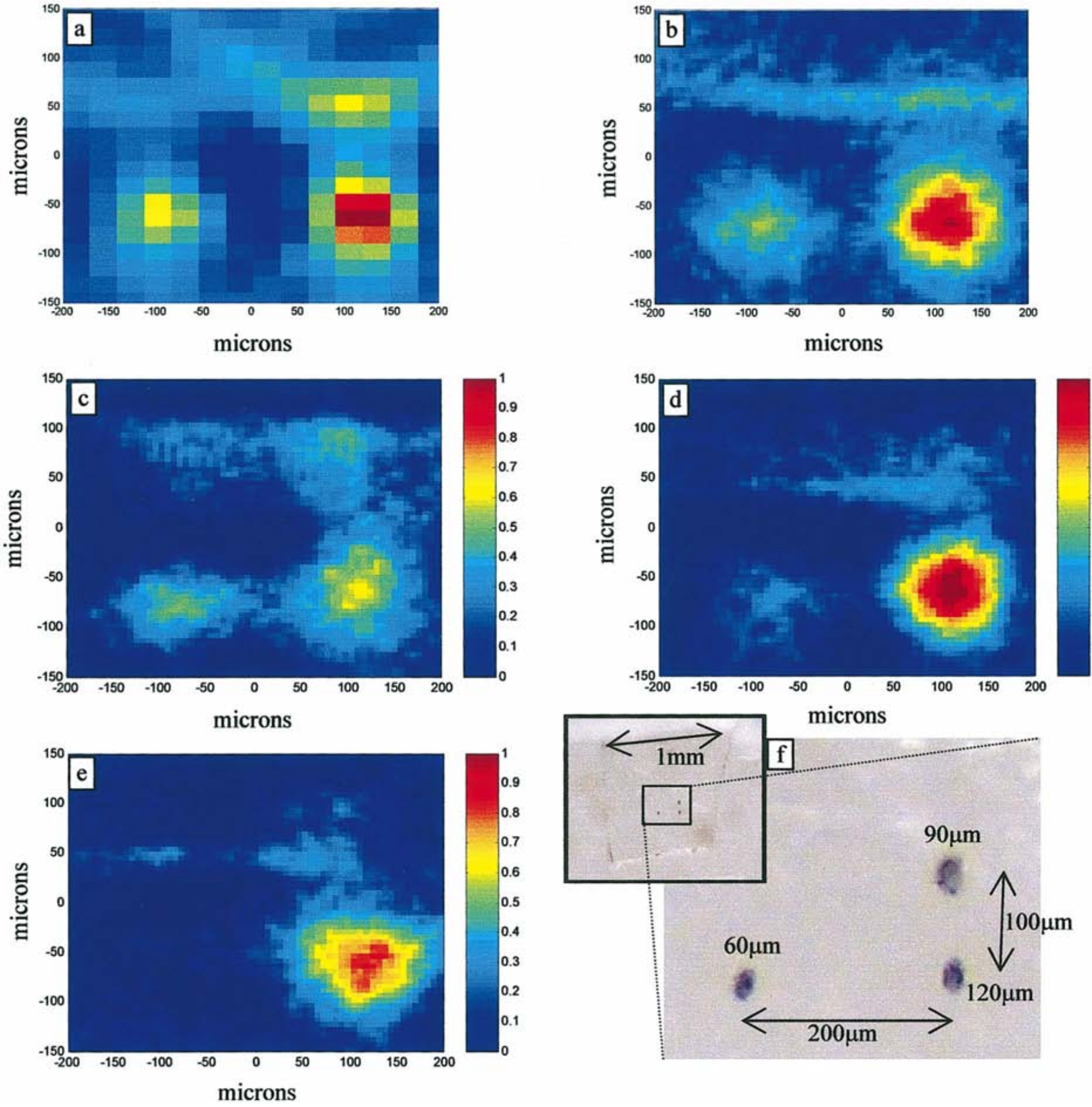

FIG. 12. (Color) 2D and 3D ESR images of LiNc–BuO radical in glass matrix. The linewidth of this radical in the partially oxygenated sample is 0.03 mT. (a) Zoom in on part of a 2D ESR image acquired with the PR method. The original image was obtained using 128 sampling points of 128 projections (in equal intervals at 0–360°), gradients of 2 T/m, time constant of 100 ms per point, and image acquisition time of 27 min. (b) A 2D ESR image of the same glass target (without any *Z*-slice selection), acquired with the MFG method, *XY* gradients of 1.2 T/m, and time constant of 0.4 s. Total image acquisition time for the 64×64 pixels is 27 min. (c) A 3D ESR image acquired with the MFG method employing *Z*-slice selection to observe only the upper part of the glass. The *X*, *Y*, and *Z* gradients were all ~1.2 T/m, microwave power ~40 μW (larger than the LiPc case due to the relatively wide linewidth of this radical), and regular modulation amplitude of ~0.05 mT. Time constant was 0.4 s, and image acquisition time (64×64 voxels) was 27 min. (d) The same as (a), but for *Z*-slice selection of the center of the glass. (e) The same as (b), but for *Z*-slice selection of the bottom of the glass. The vertical color bars represent the voxel ESR signal in arbitrary scale [but common to images (c)–(e)]. (f) Optical microscope image of the measured sample. The numbers near each radical spot represent the depth of the pit.

creasing oxygen concentration. Figure 12 presents 2D and 3D ESR images, acquired with the MFG and PR methods, of a test sample, which contains these radicals in a solid form. The sample was prepared in the following manner: A UV laser ($\lambda=193$ nm, Lumonics PM-848k excimer laser) was used to drill three small pits in a thin (150 μm) glass cover slip. The position of the center of the pits can be controlled to a high degree of accuracy (~0.2 μm) with an *XY* table. However, the geometry of the pits depends on the shape of the laser beam, which tends to be oval rather than perfectly round, and also changes along the pit depth. A high resolution optical microscope (Olympus) was used to measure the typical pit dimensions (~25–40 μm, depending on the position along the depth), and to estimate the depth of the pits [as marked on Fig. 12(f)]. The glass with the three pits was placed in a 10 mM LiNc–BuO suspension[25] and then was taken out and its surface was cleaned with a sharp knife.

The 2D images of this sample [Figs. 12(a) and 12(b)], acquired with the PR and MFG methods, show good agreement with one another and also correspond well to the optical image [Fig. 12(f)]. The apparent increase in image

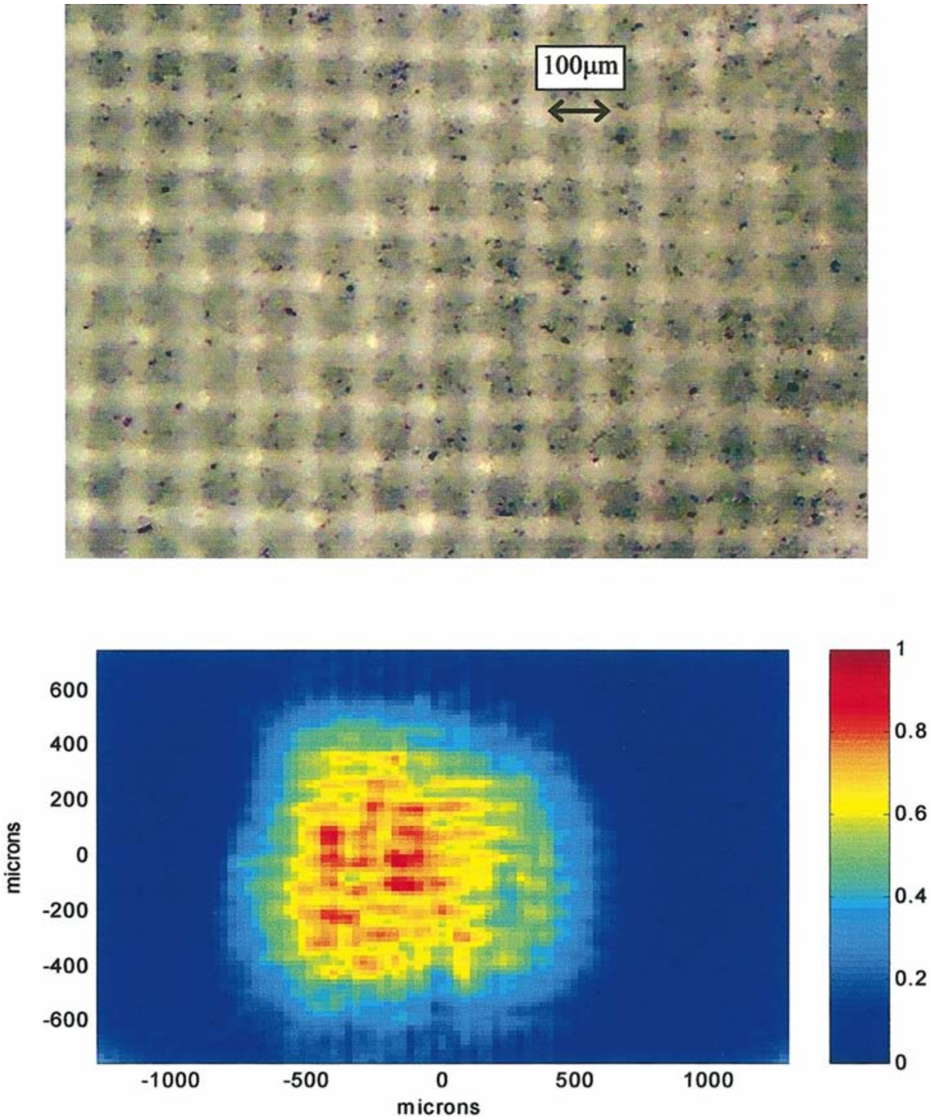

FIG. 13. (Color) Top: Optical image of LiNc–BuO liquid suspension in a thin nylon mesh. Bottom: ESR image of the liquid suspension, obtained with PR method. The gradients in X and Y were 2 T/m and regular modulation field was 0.05 mT. Image was acquired by collecting 128 projections (0–360°) with 128 sampling points at each projection, 20 ms time constant per sampling point. Total image acquisition time was 6 min. The vertical color bar represents the relative pixel ESR signal in arbitrary scale.

"noise" [as compared to the 3D images in Figs. 12(c)–12(e)] is probably due to the signal from residual radicals left on both sides of the glass (that are largely eliminated in the 3D image). One important issue that is evident from these 2D images is that the PR image has fewer pixels than the MFG image. This is due to the fact that in the PR method one has to acquire information from the entire sample and cannot collect information from only a small part of the sample (as the MFG can). In the present case, there were residual signals from the glass surface and the edges of the glass. These signals had to be collected with the PR method, which resulted in a rather large image of $\sim 2 \times 2$ mm, with only 90 $\times$ 90 pixels (after inverse Radon transform of the 128 projections, each with 128 samples[26]). This is a disadvantage for PR in microscopy applications. The 3D ESR image of the upper side of the glass [Fig. 12(c)] follows the optical image closely, but with an additional small signal that is probably due to some residual radicals that were not removed from the glass surface. Figures 12(d) and 12(e) show the gradual disappearance of the signal from two out of the three pits, due to their different depths [Fig. 12(f)], as the imaging slices observe different parts of the glass. Again, some residual signal may arise from radicals left on the upper and lower surfaces of the glass.

It is difficult to supply meaningful quantitative analysis of image SNR in this case due to the lack of a good assessment of spin density in the pits and the problem of residual radicals on the glass surface that create effective "noise." However, it is clear that this radical provides the possibility of looking at very fine details on the order of ~ 30 μm in a short acquisition time of several minutes. In terms of image resolution, the theoretical resolution for this radical, that (for the present sample) has a linewidth of ~ 0.03 mT, is ~ 36 μm. This rather low resolution is apparent in the broadening of the signal from the small pits, but still enables good separation between the pits that are separated ~ 70 μm apart (from edge to edge).

Another imaging example, which is more relevant to biological applications, involves a liquid suspension of the same LiNc–BuO radical.[25] Figure 13 shows the 2D ESR image obtained with the PR method for such a suspension (10 mM concentration) embedded within a fine nylon mesh (obtained from Goodfellow; mesh aperture 50 μm, and wire size 39 μm). The PR is the method of choice when one requires fast imaging of the entire sample in order to obtain, for example, morphological information. Following the acquisition of the PR image one can optionally observe in more detail some specific voxels within the sample (employing the MFG). The ESR image clearly shows: (1) the separation of the compartments in the mesh, and (2) that the signal is obtained only from the active area of the resonator (cf. Fig. 7). An interesting point that should be noted is that such radical suspensions are usually employed in *in vivo* imaging studies with ~1 mm resolution, and in this scale the suspension is rather uniform. However, at the 10 μm scale, the suspension is not uniform and some of the areas contain larger grains than other areas (as can also be seen in the optical image). This nonuniformity is manifested in the ESR microimage.

ACKNOWLEDGMENTS

The authors thank Professor P. Kuppusamy, Dr. N. Parinandi, and Dr. Y. Deng from the Biomedical EPR Imaging Center at Ohio State University for supplying them with samples of the LiNc–BuO radical suspensions and the deconvolution routine for the PR imaging. This research was supported by grants from NIH/NCRR and NSF chemistry.

[1] B. Blumich, *NMR Imaging of Materials. Monographs on the Physics and Chemistry of Materials* (Oxford University Press, Oxford, 2000).

[2] E. Fukushima, *NMR in Biomedicine: The Physical Basis. Key Papers in Physics; No. 2.* (American Institute of Physics, New York, 1989).

[3] D. G. Gadian, *NMR and its Applications to Living Systems*, 2nd ed. (Oxford University Press, Oxford, 1995).

[4] G. R. Eaton and S. S. Eaton, Concepts Magn. Reson. **7**, 49 (1995).

[5] G. L. He, A. Samouilov, P. Kuppusamy, and J. L. Zweier, Mol. Cell. Biochem. **234**, 359 (2002).

[6] H. M. Swartz and R. B. Clarkson, Phys. Med. Biol. **43**, 1957 (1998).

[7] K. I. Yamada, R. Murugesan, N. Devasahayam, J. A. Cook, J. B. Mitchell, S. Subramanian, and M. C. Krishna, J. Magn. Reson. **154**, 287 (2002).

[8] P. T. Callaghan, *Principles of Nuclear Magnetic Resonance Microscopy* (Oxford University Press, Oxford, 1991).

[9] M. Ikeya, Annu. Rev. Mater. Sci. **21**, 45 (1991).

[10] F. Sakran, A. Copty, M. Golosovsky, N. Bontemps, D. Davidov, and A. Frenkel, Appl. Phys. Lett. **82**, 1479 (2003).

[11] Z. Xiang and Y. Xu, Appl. Magn. Reson. **12**, 69 (1997).

[12] A. Feintuch, G. Alexandrowicz, T. Tashma, Y. Boasson, A. Grayevsky, and N. Kaplan, J. Magn. Reson. **142**, 82 (2000).

[13] A. Blank, C. R. Dunnam, P. P. Borbat, and J. H. Freed, J. Magn. Reson. **165**, 116 (2003).

[14] C. P. Poole, *Electron Spin Resonance: A Comprehensive Treatise On Experimental Techniques*, 2nd ed. (Wiley, New York, 1983).

[15] J. P. Hornak, J. K. Moscicki, D. J. Schneider, and J. H. Freed, J. Chem. Phys. **84**, 3387 (1986).

[16] J. K. Moscicki, Y. K. Shin, and J. H. Freed, J. Magn. Reson. (1969-1992) **84**, 554 (1989).

[17] S. Gravina and D. G. Cory, J. Magn. Reson., Ser. B **104**, 53 (1994).

[18] A. Feintuch, T. Tashma, A. Grayevsky, J. Gmeiner, E. Dormann, and N. Kaplan, J. Magn. Reson. **157**, 69 (2002).

[19] A. Blank, E. Stavitski, H. Levanon, and F. Gubaydullin, Rev. Sci. Instrum. **74**, 2853 (2003).

[20] P. P. Borbat, A. J. Costa-Filho, K. A. Earle, J. K. Moscicki, and J. H. Freed, Science **291**, 266 (2001).

[21] J. H. Freed, Annu. Rev. Phys. Chem. **51**, 655 (2000).

[22] T. Herrling, N. Klimes, W. Karthe, U. Ewert, and B. Ebert, J. Magn. Reson. (1969-1992) **49**, 203 (1982).

[23] T. Herrling, J. Fuchs, and N. Groth, J. Magn. Reson. **154**, 6 (2002).

[24] K. Ohno and M. Watanabe, J. Magn. Reson. **143**, 274 (2000).

[25] R. P. Pandian, N. L. Parinandi, G. Ilangovan, J. L. Zweier, and P. Kuppusamy, Free Radic Biol. Med. **35**, 1138 (2003).

[26] G. R. Eaton, S. S. Eaton, and K. Ohno, *EPR Imaging and In Vivo EPR* (CRC, Boca Raton, FL, 1991).

[27] U. Ewert and T. Herrling, J. Magn. Reson. (1969-1992) **61**, 11 (1985).

[28] A. J. denDekker and A. vandenBos, J. Opt. Soc. Am. A **14**, 547 (1997).

[29] O. Gonen and H. Levanon, J. Phys. Chem. **88**, 4223 (1984).

[30] J. S. Hyde, H. S. Mchaourab, T. G. Camenisch, J. J. Ratke, R. W. Cox, and W. Froncisz, Rev. Sci. Instrum. **69**, 2622 (1998).

[31] A. D. Poularikas, *The Transforms and Applications Handbook*, 2nd ed. (CRC, Boca Raton, FL, 2000).

[32] M. Jaworski, A. Sienkiewicz, and C. P. Scholes, J. Magn. Reson. **124**, 87 (1997).

[33] J.-M. Jin, *Electromagnetic Analysis and Design in Magnetic Resonance Imaging* (CRC, Boca Raton, FL, 1999).

[34] J. Krupka, R. G. Geyer, M. Kuhn, and J. H. Hinken, IEEE Trans. Microwave Theory Tech. **42**, 1886 (1994).

[35] J. H. Ardenkjaer-Larsen, I. Laursen, I. Leunbach, G. Ehnholm, L. G. Wistrand, J. S. Petersson, and K. Golman, J. Magn. Reson. **133**, 1 (1998).

[36] K. J. Liu, P. Gast, M. Moussavi, S. W. Norby, N. Vahidi, T. Walczak, M. Wu, and H. M. Swartz, Proc. Natl. Acad. Sci. U.S.A. **90**, 5438–5442 (1993).

[37] L. Ciobanu, D. A. Seeber, and C. H. Pennington, J. Magn. Reson. **158**, 178 (2002).

[38] Determining the resolution in magnetic resonance microscopy is far from trivial. Ideally one would like to look at a test sample consisting of two infinitely small points and to determine the minimal distance between the points that can still be resolved (i.e., the resolution). In practice, in contrast to optical methods, the signal of point-like sample will be too low to be detectable, and the actual fabrication of such a sample is a demanding task in itself. Instead, we follow here the conventional approach of NMR microscopy (Ref. 37), which observes objects of well defined finite size, where one may estimate the resolution in the image by measuring how sharp is the falloff of the signal at the sample edges, which are determined by the high resolution optical image of the same object.

[39] T. Herrling, K. U. Thiessenhusen, and U. Ewert, J. Magn. Reson. (1969-1992) **100**, 123 (1992).